

# High Purcell factor generation of coherent on-chip single photons

F. Liu <sup>†,1</sup> A. J. Brash <sup>†,1,\*</sup> J. O'Hara <sup>†,1</sup> L. M. P. P. Martins,<sup>1</sup> C. L. Phillips,<sup>1</sup> R. J. Coles,<sup>1</sup> B. Royall,<sup>1</sup> E. Clarke,<sup>2</sup> C. Bentham,<sup>1</sup> N. Prtljaga,<sup>1</sup> I. E. Itskevich,<sup>3</sup> L. R. Wilson,<sup>1</sup> M. S. Skolnick,<sup>1</sup> and A. M. Fox<sup>1</sup>

<sup>1</sup>Department of Physics and Astronomy, University of Sheffield, Sheffield, S3 7RH, United Kingdom

<sup>2</sup>EPSRC National Centre for III-V Technologies,

Department of Electronic and Electrical Engineering, University of Sheffield, Sheffield S1 3JD, UK

<sup>3</sup>School of Engineering and Computer Science, University of Hull, Hull, HU6 7RX, United Kingdom

**On-chip single-photon sources are key components for integrated photonic quantum technologies.** Semiconductor quantum dots can exhibit near-ideal single photon emission but suffer from significant dephasing in on-chip geometries owing to nearby etched surfaces. A long-proposed solution is to use the Purcell effect of an optical nanocavity to reduce the radiative lifetime to much less than dephasing timescales. However, until now only modest Purcell enhancements have been observed. Here we use resonant excitation to eliminate slow relaxation paths, revealing a highly Purcell-enhanced radiative lifetime of only 22.7 ps. This is measured by applying a novel high-time-resolution double  $\pi$ -pulse resonance fluorescence technique to a quantum dot in a waveguide-coupled photonic crystal cavity. Coherent scattering measurements confirm the short lifetime and show that the quantum dot exhibits near-radiatively-limited coherence. Under  $\pi$ -pulse excitation, the waveguide coupling enables demonstration of an on-chip, on-demand single-photon source exhibiting high purity and indistinguishability without spectral filtering.

Integrated quantum photonics has made great progress in recent years, with quantum advantage demonstrated in boson sampling and interferometer sensitivity applications [1]. However, scaling beyond the few-photon level is presently limited by large losses from the use of off-chip single-photon sources (SPSs), with the current state of the art operating at the 3-5 photon level [2–5]. Whilst SPSs have been realized on-chip using four-wave mixing [6], the very low efficiency imposes significant limitations. A solution to this issue would be to integrate an array of deterministic single-photon sources on-chip [7–14]. Among the possible candidates for such sources, semiconductor quantum dots (QDs) have been shown to offer nearly ideal performance when emitting into free space [15–18]. In particular, photon indistinguishability values, determined by the  $T_2/(2T_1)$  ratio (where  $T_1$  and  $T_2$  are the emitter lifetime and coherence time respectively), of nearly unity have been achieved [16–18].

However, the integration of QD sources into on-chip geometries has been observed to degrade the photon coherence (and hence indistinguishability). Charge noise from the etched surfaces reduces the pure dephasing time ( $T_2^*$ ) of excitons in InGaAs QDs [10, 19–21] to well below typical exciton lifetimes ( $T_1$ ) of  $\sim 1$  ns [22]. Since  $1/T_2 = 1/(2T_1) + 1/T_2^*$ , a long-proposed [21, 23, 24] approach to negating the effects of the dephasing is to use the Purcell effect [23, 25, 26] of a photonic crystal cavity (PhCC) [27, 28] to enhance the radiative emission rate  $1/T_1$ . The Purcell factor ( $F_P$ ) is determined by the properties of the cavity and the overlap between the QD and the cavity mode. In principle, high  $F_P$  values could be easily obtained by fabricating cavities with a high  $Q$ -factor and small mode volume such as PhCCs. How-

ever, previously reported  $F_P$  values have reached only  $\sim 10$  [26, 29–32], over an order of magnitude smaller than the maximum theoretical value. Most studies attribute the large discrepancy to poor spatial overlap between the QD and the cavity mode [33] or insufficient detector time resolution [30]. Although a  $F_P$  value of 28 ( $T_1 = 53$  ps) was reported [34], the  $T_1$  value in this work was indirectly obtained from a multiple free-parameter fit of a two-photon interference measurement rather than a direct lifetime measurement.

In this paper we clearly show that larger Purcell enhancements can be achieved and that they successfully overcome dephasing of the emission. This results in close to radiatively-limited coherence, allowing demonstration of a high-performance on-chip single-photon source with on-demand operation. To achieve this, we use pulsed resonant excitation and employ a waveguide-coupled H1 PhCC in a *p-i-n* diode containing InGaAs QDs [35, 36]. To be able to measure the strongly Purcell-enhanced exciton radiative recombination rate beyond the instrument response function (IRF) of the fastest single-photon avalanche diodes (SPADs), we develop a double  $\pi$ -pulse resonance fluorescence (DPRF) technique. Using this technique, we observe a  $T_1$  as short as  $(22.7 \pm 0.9)$  ps. Comparing this to ensemble lifetimes measured on the same chip gives a record-high  $F_P$  value of 42 for a QD in a nanocavity. The short  $T_1$  is independently verified by measuring the resonant Rayleigh scattering (RRS) from the QD. The large Purcell enhancement leads to a near-unity  $T_2/(2T_1)$  ratio, resulting in near-transform-limited on-chip single-photon emission even in the presence of significant pure dephasing. Finally, we demonstrate a high-performance on-chip electrically tunable SPS by ex-

citing the QD with a resonant  $\pi$ -pulse and detecting the on-chip QD emission from the end of the waveguide. The source operates on-demand at very low excitation powers ( $\sim 5$  nW) and exhibits a high degree of photon purity (87 %) and indistinguishability ( $79.7 \pm 5.9$ ) without any spectral filtering. The short photon wave packet duration (22.7 ps) implies high potential single-photon emission rates of  $\sim 10$  GHz, crucial for realistic on-chip demultiplexing of the photons, another process that is currently performed off-chip [4, 5].

## SAMPLE DESIGN AND CHARACTERIZATION

Including the detuning and spatial overlap of the QD with respect to the cavity mode,  $F_P$  is given according to [26]:

$$F_P = \frac{T'_1}{T_1} = \frac{3Q}{4\pi^2 V_m} \frac{\Delta\omega_{\text{cav}}^2}{4(\omega - \omega_{\text{cav}})^2 + \Delta\omega_{\text{cav}}^2} \frac{|\vec{\mu} \cdot \vec{E}(\vec{r}_0)|^2}{|\vec{\mu}|^2 |\vec{E}_{\text{max}}|^2} \quad (1)$$

where  $T'_1$  is the exciton radiative lifetime in the absence of a cavity;  $Q$  is the quality factor of the cavity and  $V_m$  its volume in cubic wavelengths  $(\lambda/n)^3$ ;  $\omega$ ,  $\omega_{\text{cav}}$  and  $\Delta\omega_{\text{cav}}$  denote the frequency of the exciton transition, cavity resonance and the full width at half maximum (FWHM) of the cavity mode;  $\vec{\mu}$ ,  $\vec{E}(\vec{r}_0)$  and  $\vec{E}_{\text{max}}$  represent the transition dipole moment, the electric field at the QD position and the maximum electric field.

In order to obtain a high  $F_P$  value across a large QD tuning range, we integrate the QD into an H1 PhCC with small mode volume ( $V_m \approx 0.63 (\lambda/n)^3$ ) and relatively-low  $Q$  (see cross-sectional view in Fig. 1(a) and top view in Fig. 1(b)). The cavity has two orthogonally linearly polarized fundamental modes (M1 ( $Q = 540$ ) and M2 ( $Q = 765$ )) which are observed in the high-power photoluminescence (PL) spectra (grey lines in Fig. 1(c)). The upper theoretical limit of the  $F_P$  value is 65 for the M1 mode (see Supplementary Information (SI), section III). In order to extract the photons from the cavity and guide them on-chip, we integrate two W1 photonic crystal waveguides with the cavity. Each is coupled to one cavity mode [35, 36] and terminated with an out-coupler. The coupling efficiency between the M1 mode and the waveguide is 41 % (see SI, section I), comparable to the coupling efficiency ( $\sim 66\%$ ) between micropillar cavities and the first lens [18, 37]. Integrating the whole photonic crystal structure into a *p-i-n* diode allows tuning of the neutral exciton ( $X$ ) (see SI, section II) by  $\sim 5$  meV via the quantum-confined Stark effect (see insert in Fig. 1(c)). Clear enhancement of the PL intensity is observed when the  $X$  is tuned to be resonant with the M1 cavity mode.

To investigate the  $F_P$  value in our sample, we first measure the radiative lifetime of the exciton resonant with

the M1 cavity mode using a fast SPAD. The PL decay time ( $(262 \pm 3)$  ps, blue line in Fig. 1(d)) measured under above-barrier excitation is shortened by a factor of  $\sim 4$  compared with that of ensemble QDs ( $T'_1 = (945 \pm 3)$  ps, green line) outside the photonic crystal. Such an enhancement factor is typical compared with those reported in previous literature [26, 29–32]. However, under resonant excitation, the PL decay time is further shortened by at least a factor of 6 (to  $(46.2 \pm 1.2)$  ps without deconvolution, red line), a value limited by the instrument response function of the SPAD (FWHM = 60 ps, black line). We attribute the large difference of the PL decay time under different excitation conditions to a long carrier relaxation time from higher energy states to the lowest exciton state [38–41], supported by simulations (see SI, section VI(B)). Under non-resonant excitation, the long carrier relaxation time masks the real  $F_P$  and limits the indistinguishability of QD SPSs [23, 24]. This observation implies that in the case of strong Purcell enhancement,  $T_1$  can only be accurately measured when the exciton is populated much faster than the radiative recombination rate, in this case by resonant excitation. In addition, since in our sample  $T_1$  cannot be clearly resolved by the fastest SPADs available, a technique with higher time-resolution is essential to determine  $T_1$ .

## FAST RADIATIVE DECAY MEASURED USING DOUBLE $\pi$ -PULSE RESONANCE FLUORESCENCE TECHNIQUE

To measure  $T_1$  accurately, we develop a DPRF technique with a time resolution ultimately limited by the laser pulse width ( $\tau_L = 13$  ps) (see *Methods*, and SI, section VI(c)), making it possible to measure a  $T_1$  much shorter than the time resolution of SPADs. Fig. 2(a) shows the schematic of the experimental setup. The QD is excited by two linearly polarized resonant laser pulses with variable separation and the emission is dispersed by a spectrometer and recorded by a charge-coupled-device (CCD) camera. The reflected laser is suppressed using a modulated cross-polarization scheme (details in *Methods*).

The principle of the DPRF technique is illustrated in Fig. 2(b). The QD can be treated as a two-level system consisting of a crystal ground state (CGS)  $|0\rangle$  and an exciton state  $|X\rangle$  with a total population of 1. At  $t = 0$ , a laser pulse with a pulse area  $\Theta = \pi$  coherently drives the QD from  $|0\rangle$  to  $|X\rangle$ , creating an  $X$  population close to 1. The pulse area  $\Theta$  is calibrated by performing a Rabi oscillation measurement [42–44] (Fig. 2(c)). Before the second pulse arrives, the exciton population radiatively decays to  $C_X = e^{-\Delta t/T_1}$  via spontaneous emission (SE), where  $\Delta t$  is the inter-pulse delay. The probability of photon emission up to time  $\Delta t$  is equal to  $(1 - C_X)$ . At  $t = \Delta t$ , the second  $\pi$ -pulse

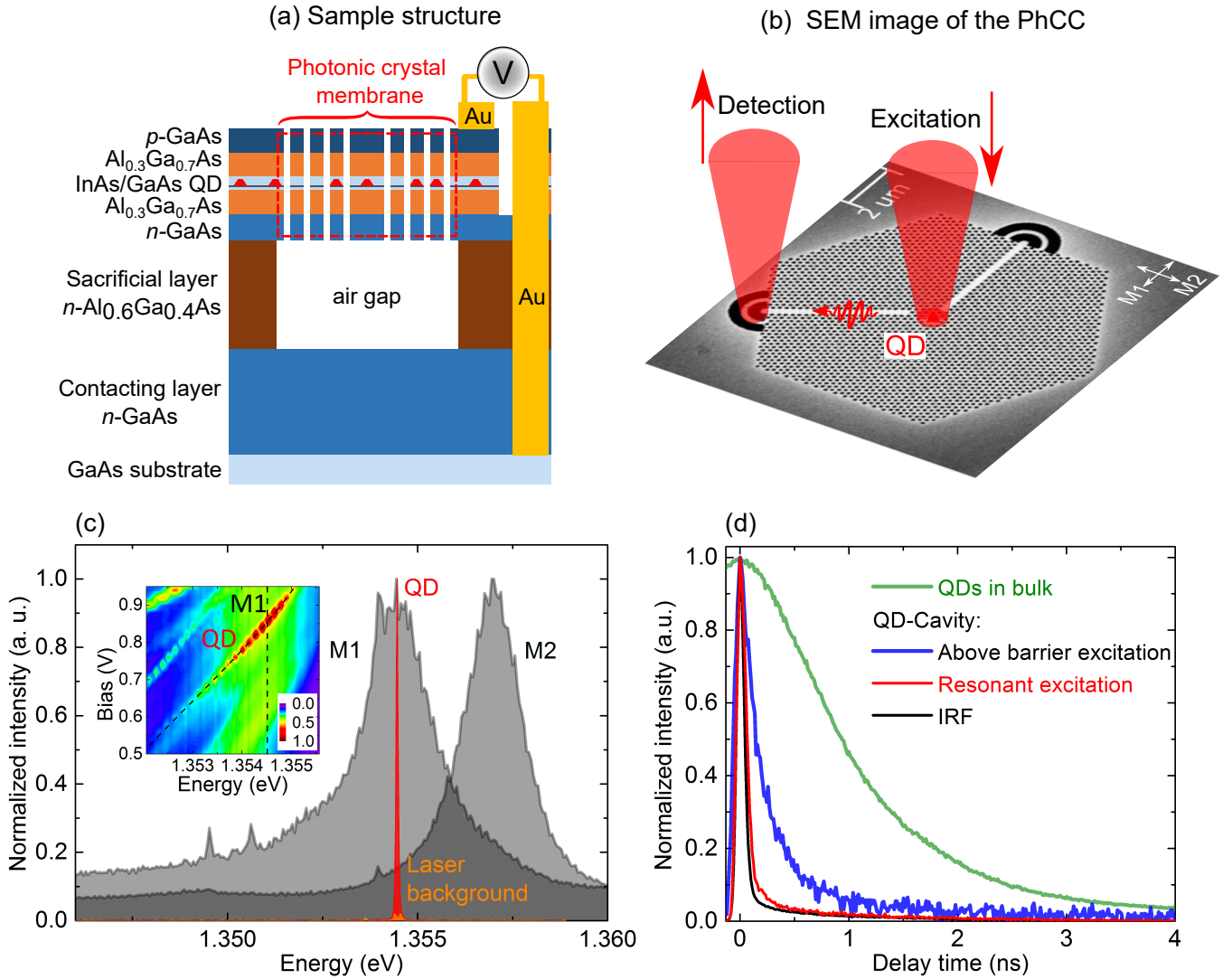


FIG. 1. (a) Sample structure - a photonic crystal membrane fabricated on a *p-i-n* diode structure containing InGaAs QDs. (b) SEM image (top view) of the waveguide-coupled QD-H1 PhCC system. When operated as an on-chip SPS (see Fig. 4), the QD is excited via the cavity and the single-photon emission is collected from the out-coupler. All other measurements are performed by collecting directly from the cavity to maximize the intensity of the RF signal. (c) Gray: Normalized high power PL spectra of the sample under above barrier excitation ( $\lambda_{\text{exc}} = 802$  nm). Two orthogonally linearly polarized modes (M1 and M2) are observed when detecting with H and V polarization respectively. Red: Single QD emission measured with resonant pulsed excitation. The laser background (orange) can be measured by detuning the QD from the laser and is  $>20$  times weaker. Insert: Normalized low power PL of the sample as a function of the bias and energy under above barrier excitation. The neutral exciton is electrically tuned by 5.2 meV from bias = 0.2 to 0.93 V (see the oblique dashed line). Maximum Purcell enhancement of the QD emission is observed around 0.83 V where the QD is resonant with the M1 mode (vertical dashed line). (d) Normalized PL decay of the QD ensemble in bulk measured with above barrier excitation (green) and that of the QD in cavity measured under above barrier (blue) and resonant (red) excitation at bias = 0.83 V. Black: Instrument response function (FWHM = 60 ps).

exchanges the populations of  $|0\rangle$  and  $|X\rangle$ . The exciton population is now  $(1 - C_X)$  which subsequently decays fully to the ground state, again giving a photon emission probability of  $(1 - C_X)$ . At small  $\Delta t \leq \tau_L$ , optical interference occurs due to the temporal overlap of the pulses. Away from this region, the total RF intensity ( $I_{\text{RF}}$ ) measured in the DPRF measurement is proportional to  $2(1 - C_X) = 2(1 - e^{-\Delta t/T_1})$ . Hence  $T_1$  can be

extracted by fitting  $I_{\text{RF}}$  as a function of  $\Delta t$  with a single exponential function.

Fig. 2(d) shows the result of the DPRF measurement at QD-cavity detuning  $\Delta E = 0$ .  $I_{\text{RF}}$  recovers with  $\Delta t$  on the timescale of the exciton radiative lifetime. Fitting the curve with a single exponential function yields a  $T_1$  of  $22.7 \pm 0.9$  ps, much smaller than previously reported values [4, 17, 18, 26, 29–32, 45]. This corresponds to a

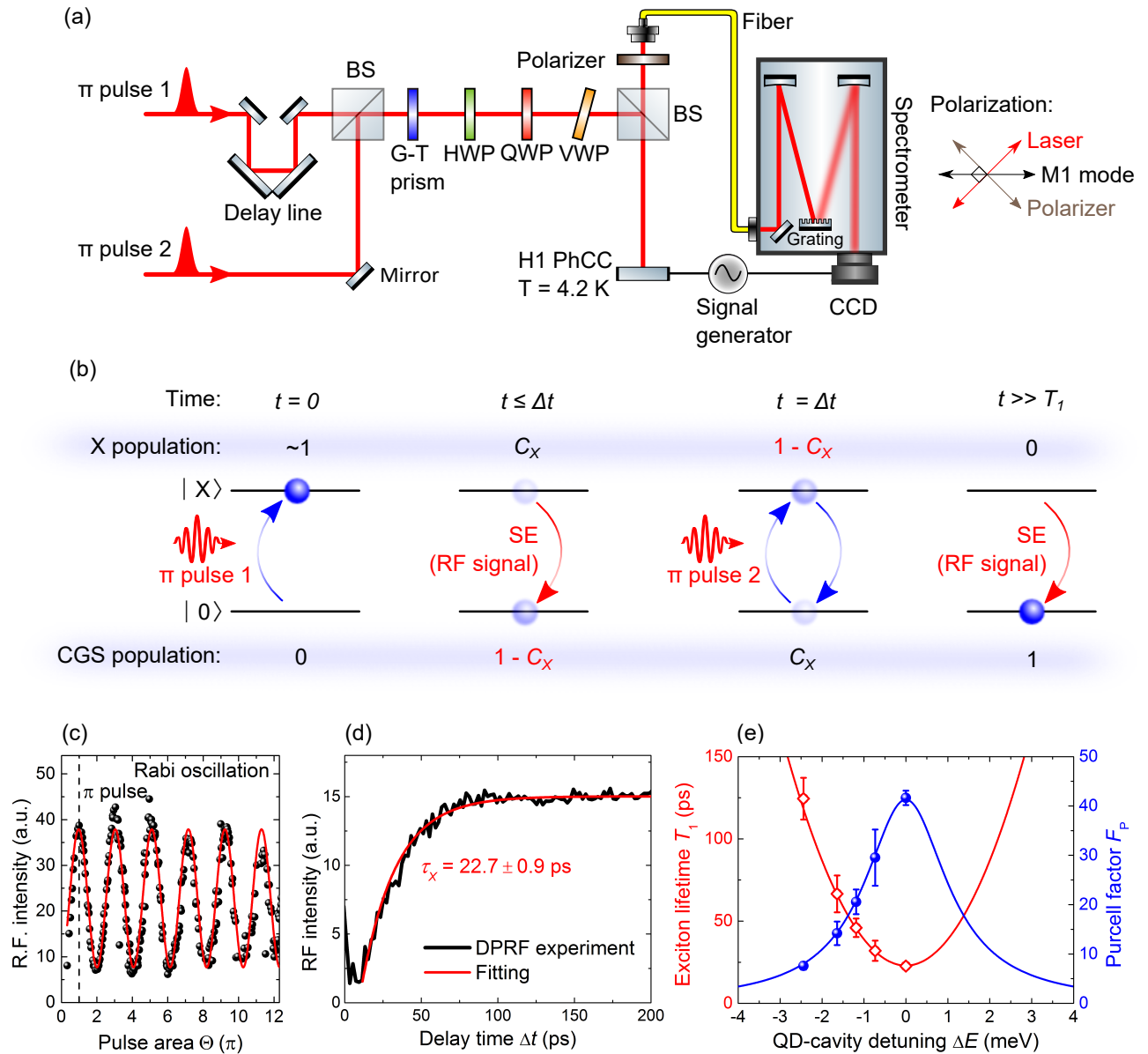


FIG. 2. (a) The experimental setup for the double  $\pi$ -pulse resonance fluorescence (DPRF) technique (see details in *Methods*). (b) The principle of the DPRF technique. SE: Spontaneous emission. (c) RF intensity of the QD as a function of the pulse area  $\Theta$  of a single pulse, showing Rabi oscillations (red line - sine fit).  $\Theta = \mu/\hbar \int_{-\infty}^{+\infty} E(t)dt$ , where  $\mu$  and  $E(t)$  denote the transition dipole moment and the laser field. (d) DPRF measurement: The RF intensity as a function of the time delay  $\Delta t$  between the  $\pi$ -pulses. Fitting (red) with a single exponential function gives an exciton radiative lifetime of  $(22.7 \pm 0.9)$  ps. (e) The dependence of  $T_1$  (red diamonds) and  $F_P$  (blue dots) on the QD-cavity detuning  $\Delta E = E_X - E_c$ , where  $E_X$  and  $E_c$  are the energies of the exciton and cavity resonances respectively. Solid lines: Simulations using eq. 1.

record-high Purcell factor for a QD-nanocavity system of 42 (for  $T'_1 = 945$  ps). The RF signal saturates at a pulse separation of around 100 ps in Fig. 2(d), indicating potential repetition rates as high as 10 GHz (see SI section VI(C)). Unlike for slower sources, on-chip delays of  $\sim 100$  ps can readily be realized [46], paving the way for on-chip time demultiplexing which is an important requirement for integrated photonic circuits.

Detuning the QD away from the cavity resonance in-

creases (decreases)  $T_1$  ( $F_P$ ) (see Fig. 2(e)). This trend is well reproduced by eq. 1 with the cavity linewidth (2.5 meV) extracted from the PL spectra (see Fig. 1(c)) and a spatial overlap of  $\sim 80$  %, providing additional evidence that the short  $T_1$  is a consequence of a large Purcell enhancement.

Our findings demonstrate three advantages of low- $Q$  cavities for on-chip SPSs. Firstly, although the QD-cavity coupling strength ( $\hbar g$ ) estimated from the  $F_P$

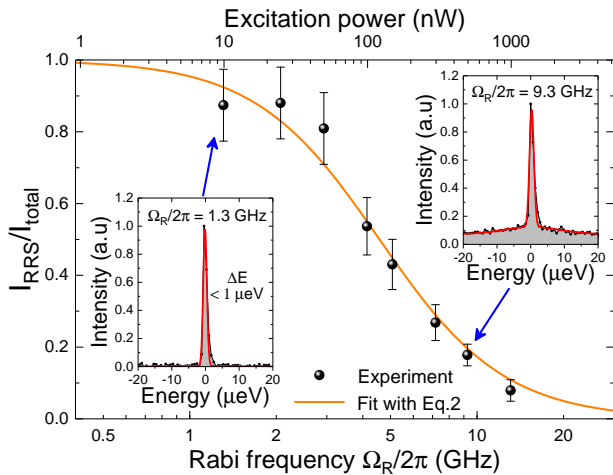


FIG. 3. Plot of the ratio of the coherently scattered laser photons ( $I_{\text{RRS}}$ ) to the total scatter ( $I_{\text{total}} = I_{\text{RRS}} + I_{\text{SE}}$ ) as a function of Rabi frequency and CW excitation power. Orange line: Fit using eq. 2. Insets: High resolution spectra of the QD emission under weak (left) and strong (right) CW resonant driving measured with a Fabry-Pérot interferometer. Red lines: Fits of the RRS and SE (see SI, section V(B)).

value is as large as 135  $\mu\text{eV}$  (see SI, section III), the low  $Q$  ensures the system remains in the weak coupling regime, as required for efficient coherent single-photon emission. Secondly, the large  $g$  results in a cavity photon number  $\ll 1$  at QD saturation [47, 48], minimizing the laser background in the waveguides. Thirdly, the high  $F_{\text{P}}$  ( $> 30$ ) and low on-chip background may be maintained within a large tuning range ( $\sim 1.4$  meV), giving an electrically-tunable source of coherent on-chip single photons.

### RESONANT RAYLEIGH SCATTERING

To further verify the short  $T_1$  and probe the coherence of the emitter, we switch to resonant continuous-wave (CW) excitation and investigate the coherent scattering from the QD, which is highly sensitive to the  $T_2/(2T_1)$  ratio. The emission from a single quantum emitter in the small Rabi frequency limit ( $\Omega_{\text{R}}^2 \ll 1/(T_1 T_2)$ ) is dominated by RRS provided  $T_2 > T_1$  [49–53]. These coherently scattered photons are anti-bunched on the timescale of the emitter lifetime but retain the linewidth (and thus coherence) of the laser. Applied to QDs, this approach allows on-chip generation of single photons whose coherence significantly exceeds the radiative limit of the SE process. The ratio of the RRS intensity to the total (RRS + SE) intensity is given by [52]:

$$\frac{I_{\text{RRS}}}{I_{\text{total}}} = \frac{T_2}{2T_1} \times \frac{1}{1 + T_1 T_2 \Omega_{\text{R}}^{-2}}. \quad (2)$$

Eq. 2 demonstrates that reducing  $T_1$  through a large  $F_{\text{P}}$  value leads to an improved fraction of RRS. The first term implies that a high fraction of RRS may only be attained for an emitter operating close to the radiative limit ( $T_2 = 2T_1$ ) whilst the second term leads to increasing SE as  $\Omega_{\text{R}}^2 \rightarrow 1/(T_1 T_2)$ , limiting the coherent scattering rate in the regime where RRS dominates. In our experiments the driving laser intensity is converted to  $\Omega_{\text{R}}$  by measuring the power-dependent splitting of the Mollow triplet (see SI, section V(C)).

To demonstrate these advantages, resonant CW excitation is used and the QD is tuned into resonance with the M1 cavity mode. High resolution spectroscopy is performed using a scanning Fabry-Pérot interferometer (FPI). Typical spectra are shown in the insets of Fig. 3. At high driving strengths (right-hand inset), the spectrum consists of a sub- $\mu\text{eV}$  (FPI resolution-limited) component from RRS with a broad contribution from SE which vanishes as expected at lower driving strengths (left-hand inset). By fitting the spectra, the ratio  $I_{\text{RRS}}/I_{\text{total}}$  may be evaluated as a function of  $\Omega_{\text{R}}$  as in Fig. 3.

A fit using eq. 2 is included in Fig. 3 as an orange line and gives  $T_1 = (24.6 \pm 1.6)$  ps and  $T_2 = (49.2 \pm 5.4)$  ps, indicating that the emitter has very close to radiatively-limited coherence, and providing an independent measure of the short radiative lifetime. At a Rabi frequency  $\Omega_{\text{R}}/(2\pi)$  of 2 GHz, the RRS fraction is  $(87.4 \pm 11.1)$  % with a calculated waveguide count-rate of 11.5 MHz and a signal-to-background ratio (SBR)  $> 150 : 1$  (see SI, section V(a)). The high photon coherence and cavity-enhanced photon emission rate renders these photons ideal for on-chip applications such as probabilistic logic gates [54, 55] and generating distant entanglement between spins [56, 57]. However, the RRS limit of  $\Omega_{\text{R}}^2 \ll 1/(T_1 T_2)$  means that even if the laser is modulated to produce optically triggered single photons, the emission probability per laser pulse is  $< 10$  % [58]. In order to further increase the photon emission rate and generate single photons on-demand we now study our device under  $\pi$ -pulse resonant excitation where the peak Rabi frequencies are much higher.

### ON-CHIP ON-DEMAND SINGLE-PHOTON SOURCE

QDs driven by resonant  $\pi$ -pulses have proven to be an excellent source of single photons owing to their high purity, indistinguishability and on-demand operation [16–18]. Such performance would be highly desirable for an on-chip single-photon source. However, to date all QD SPSs driven by resonant  $\pi$ -pulses have emitted into free-space. By exciting on the cavity and collecting from the waveguide of our device (see Fig. 1(b)), we observe nearly background-free pulsed RF, realising a resonantly-driven

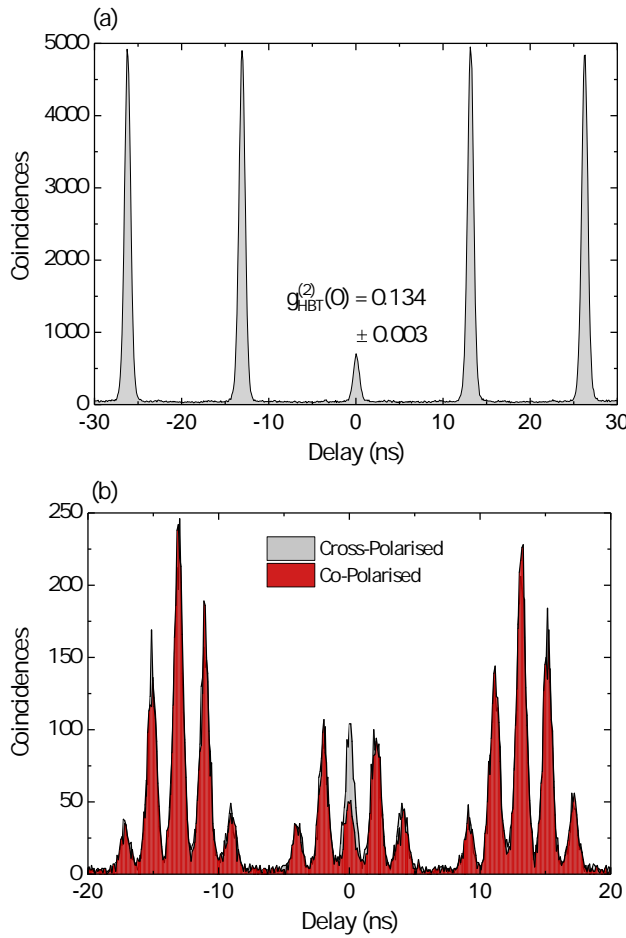


FIG. 4. Second-order correlation measurements of the waveguide-coupled QD emission under resonant  $\pi$ -pulse excitation. (a) Hanbury Brown and Twiss measurement of single-photon purity. (b) Hong-Ou-Mandel measurement of interference visibility for photons emitted 2 ns apart. The red and blue data show coincidence counts for co- and cross-polarization of the two interferometer arms respectively (see *Methods* and SI, section VII for further details).

on-chip on-demand SPS.

To characterize the performance of our device under pulsed excitation, we perform interferometry and second-order correlation measurements to determine the emission purity and indistinguishability. Owing to the use of efficient, resonant excitation and the spatial separation of our excitation and collection spots, RF is observed with a SBR  $> 20 : 1$  under  $\pi$ -pulse excitation with no emission from other transitions. As a result, we are able to perform correlation measurements using only polarization filtering, unlike in many previous studies where lossy narrow-band spectral filtering is used to further reduce residual scattered laser and remove the incoherent emission of the QD phonon sideband [16–18]. To achieve this, the collection polarizer is matched to the waveguide emission, giving an indication of the true on-chip per-

formance of the device (limited by residual collection of scattered excitation light).

To characterize the purity of the source, a Hanbury Brown and Twiss (HBT) correlation measurement is performed under resonant  $\pi$ -pulse excitation. The results are shown in Fig. 4(a) where the area of the time-zero peak gives a purity  $(1 - g_{HBT}^{(2)}(0))$  of  $86.6 \pm 0.3\%$ . This value is similar to unfiltered purities measured for off-chip geometry QDs with resonant pulsed excitation [17, 59].

Using a fiber Mach-Zehnder interferometer (see SI, section VII), Hong-Ou-Mandel (HOM) interferometry is performed to determine the indistinguishability of photons emitted with 2 ns separation (Fig. 4 (b)). This value is limited by the SPAD response time (see *Methods*) and corresponds to 25 excitation cycles of the source at RF saturation. We note that indistinguishability has been shown to reduce as the photon separation reaches the timescales of dephasing mechanisms [60, 61].

The HOM measurement yields a raw visibility of 52.3 %. After correction for the  $g_{HBT}^{(2)}(0)$  value and the interferometer properties (see SI, section VII), a value of  $V = (79.7 \pm 5.9)\%$  is extracted. This value significantly exceeds the visibility measured through an off-chip spectral filter ( $V = 62\%$ ) for pulsed  $p$ -shell excitation of a QD-in-waveguide source [24]. The improved  $V$  illustrates the benefits of the resonantly-driven high-Purcell approach, in particular the absence of timing jitter due to relaxation processes [23]. The low  $Q$  of the cavity also allows the source to be electrically tuned whilst retaining the coherence and high photon emission rate advantages of a significant Purcell factor.

Recent studies have indicated that the unfiltered visibility of single photons from non Purcell-enhanced In-GaAs QDs at 4.2 K is limited to around 80 % by incoherent phonon sideband emission [59, 62]. This can be improved without the losses of an external filter by placing the QD in a resonant high- $Q$  cavity [62]. In this sample, whilst there is a high Purcell factor, the relatively low  $Q$  means that the filtering effect is weaker, introducing an upper bound on the visibility of  $\sim 90\%$  [62]. The  $V$  observed in our measurements is also limited by collection of residual scattered excitation light and uncertainty in the temporal overlap of the short photon wavepackets in the interferometer. These factors indicate that our measurement is a lower-bound to attainable on-chip performance. Lengthening the waveguides to reduce collection of laser scatter and optimizing the cavity-waveguide coupling presents a path to increasing the measured SBR and brightness in future devices.

## CONCLUSION AND OUTLOOK

In this article we measure an exciton radiative lifetime of only 22.7 ps due to a very large Purcell enhancement in a photonic crystal cavity. This is revealed with a

novel high-time-resolution double  $\pi$ -pulse resonance fluorescence technique, and corresponds to a record-high Purcell factor of 42 for a QD-nanocavity system. On-demand single photons from the cavity are efficiently channeled into a waveguide with minimal laser background, allowing the device to operate as an on-chip SPS. The large Purcell enhancement enables the QD to exhibit nearly radiatively-limited coherence even in the presence of nearby etched surfaces that typically significantly reduce coherence times in photonic nanostructures [10, 19–21]. Additionally, the small  $T_1$  enables source repetition rates  $\sim 10$  GHz which are compatible with on-chip delays for time demultiplexing [46]. Other important QIP proposals such as fast single-photon switching [63] and photonic cluster state generation [64, 65] can also benefit significantly from short radiative lifetimes.

Under weak resonant CW excitation, a very high fraction of RRS is observed, indicating lifetime-limited emitter coherence and providing an on-chip source of subnatural linewidth single photons. With pulsed resonant excitation, the device operates on-demand with high single-photon purity (86.7 %) and indistinguishability (79.7%) demonstrated without spectral filtering. In addition, the emission may be electrically tuned whilst retaining the benefits of a high Purcell factor. This performance exceeds previous QD-based on-chip sources that use non-resonant pulsed excitation [24] and requires orders of magnitude less excitation power and space than existing spontaneous four-wave mixing sources [6] with the benefits of on-demand operation and a much higher photon generation rate. As such, our on-chip source marks a major step forward in fully-integrated chip devices for quantum photonics, building on the excellent progress already made in integrated nano-optics and detectors on GaAs [21].

## METHODS

### DPRF Setup

The QD is resonantly driven by a pair of 13 ps pulses derived by splitting and shaping a broad 100 fs laser pulse generated from a Ti:Sapphire laser with repetition rate 76 MHz. This pulse length is chosen to maximise the signal-to-background ratio (by reduced spectral width) whilst remaining shorter than the QD radiative lifetime. A cross-polarization configuration is adopted to detect the resonant QD emission, as shown in Fig. 2(a). The polarization direction of the laser pulses is initially defined by a Glan-Taylor prism, rotated by a half-wave plate (HWP) and reflected by a non-polarizing beam splitter (BS). The combination of the HWP and the BS allows us to easily set the polarization of the laser pulse. For these measurements, the laser pulses are 45° polarized with respect to the M1 cavity mode. The reflected

laser is filtered out by a cross-polarizer. The distortion of the polarization of the laser by all optical components in the excitation *and* detection paths is corrected by a quarter wave-plate and an additional tunable wave-plate with quarter-wave phase retardation. The spectrally-integrated signal to background ratio under  $\pi$ -pulse excitation is  $\sim 20:1$ , smaller than that ( $\sim 150:1$ ) under CW excitation (laser power = 25 nW) due to difficulties in rejecting a broadband laser pulse using polarisation. To fully separate the RF signal from the laser background in the DPRF measurement, the bias of the diode is modulated with a frequency of 11 Hz to move the QD in and out of resonance with the laser pulse. The laser background can be fully removed by subtracting the two spectra from each other (see example QD and background spectra in Fig. 1(c)).

### SPAD Lifetime Measurements

The single-photon avalanche diode (SPAD) lifetime measurements are performed using the optical setup of the DPRF measurement. For the ensemble lifetime of QDs outside the photonic crystal, the excitation is provided by the unshaped ( $\sim 100$  fs) output of the Ti:S laser operating at  $\lambda = 780$  nm. A 900 nm long-pass filter is inserted after the detection polarizer to remove the laser from the detection path. The collection fiber is connected directly to a SPAD operating in Geiger mode with a Gaussian IRF of FWHM 350 ps. A time-correlated single-photon counting module (TCSPCM) synchronized with the laser pulse train records the arrival times of individual photons to produce the decay curves. For the remaining lifetime measurements the zero-phonon line is filtered through the spectrometer ( $\sim 80$   $\mu$ eV bandwidth) before passing to a different SPAD with higher time resolution (IRF  $\sim 60$  ps with a weak, longer tail) and being analyzed by the TCSPCM as before. For the above-band lifetime measurement the excitation pulse is again supplied by the unshaped laser whilst the resonant  $\pi$ -pulse is provided by a single pulse-shaper as in the DPRF measurement.

### Resonant Rayleigh Scattering

For the RRS measurements a narrow-linewidth ( $< 50$  kHz) continuous-wave tunable Ti:S laser provides the excitation source. The optical setup is as for the DPRF measurements except that the emission is passed to the exit slit of the spectrometer and filtered as previously described. The emission then passes through a scanning Fabry-Pérot interferometer (FPI) and is detected with a SPAD. The FPI is swept by a function generator which also provides a synchronization signal to the TCSPCM,

allowing conversion from SPAD detection time to spectral position.

### Correlation Measurements

To perform the correlation measurements, the optical setup employed for the DPRF measurements is again used. The detection fiber is connected directly (bypassing the spectrometer) to a fiber Mach-Zehnder interferometer with one arm incorporating a  $\lambda/2$  wave-plate and the other an additional length of fiber corresponding to a 2 ns delay. The two output ports of the interferometer are connected to a pair of single-photon avalanche photodiodes (combined Gaussian IRF has FWHM 860 ps), which in turn are fed to the TCSPCM in order to measure the number of coincidence counts. Further details of the interferometer are contained within the SI, section VII. For HBT measurements, a single  $\pi$ -pulse per laser cycle (13.2 ns) is applied to the sample and the detection fiber is connected directly to the second fiber splitter of the interferometer. For HOM measurements the full interferometer is used and a pair of  $\pi$ -pulses is applied to the sample as in the DPRF experiment. The pulse separation is fixed at 2 ns to match the interferometer delay.

### ACKNOWLEDGEMENT

This work was funded by the EPSRC (UK) Programme Grants EP/J007544/1 and EP/N031776/1. The authors thank A. Ul-Haq, J. Iles-Smith, and G. Buonaiuto for useful discussions.

### AUTHOR CONTRIBUTIONS

F.L. and A.J.B. designed and oversaw the experimental program. A.J.B., L.M.P.P.M. and F.L. developed the DPRF technique and carried out the measurements. J.O'H., L.M.P.P.M., A.J.B. and F.L. performed the SPAD lifetime measurements. J.O'H. and A.J.B. performed the RRS measurements with additional input from N.P.. A.J.B., J.O'H., L.M.P.P.M., F.L. and C.L.P. performed the pulsed correlation measurements. J.O'H. performed the master equation simulations of the system. R.J.C. designed the photonic structures and performed FDTD simulations of them. C.B. and I.E.I. performed initial characterisation of the sample. E.C. grew the quantum dot wafer whilst B.R. fabricated the photonic nanostructures and processed the QD wafer into diodes with assistance from C.B.. L.R.W, I.E.I., M.S.S and A.M.F. provided supervision and expertise. F.L., A.J.B., J.O'H. and A.M.F. wrote the manuscript with input from all authors.

### ADDITIONAL INFORMATION

Supplementary information is available in the online version of the paper. Reprints and permission information is available online at URL. Correspondence and requests for materials should be addressed to a.brash@sheffield.ac.uk. F. Liu's present address: JARA-Institute for Quantum Information, RWTH Aachen University, D-52074 Aachen, Germany; N. Prtljaga's present address: Gooch & Housego (Torquay), Broomhill Way, Torquay, TQ2 7QL, United Kingdom.

### COMPETING INTERESTS

The authors declare that they have no competing financial interests.

\* Email:a.brash@sheffield.ac.uk

† F. Liu, A.J. Brash and J. O'Hara contributed equally to this work.

- [1] Aaronson, S. & Arkhipov, A. The Computational Complexity of Linear Optics. In *The 43rd annual ACM symposium on Theory of Computing, STOC '11*, 333–342 (ACM Press, New York, 2011).
- [2] Tillmann, M. *et al.* Experimental boson sampling. *Nature Photonics* **7**, 540–544 (2013).
- [3] Broome, M. A. *et al.* Photonic Boson Sampling in a Tunable Circuit. *Science* **339**, 794 – 798 (2013).
- [4] Wang, H. *et al.* High-efficiency multiphoton boson sampling. *Nat Photon* advance online publication.
- [5] Loredo, J. C. *et al.* Boson Sampling with Single-Photon Fock States from a Bright Solid-State Source. *Physical Review Letters* **118**, 130503 (2017).
- [6] Silverstone, J. W. *et al.* On-chip quantum interference between silicon photon-pair sources. *Nat Photon* **8**, 104–108 (2014).
- [7] Laucht, A. *et al.* A Waveguide-Coupled On-Chip Single-Photon Source. *Phys. Rev. X* **2**, 11014 (2012).
- [8] Lodahl, P., Mahmoodian, S. & Stobbe, S. Interfacing single photons and single quantum dots with photonic nanostructures. *Reviews of Modern Physics* **87**, 14352–14366 (2015).
- [9] Lund-Hansen, T. *et al.* Experimental Realization of Highly Efficient Broadband Coupling of Single Quantum Dots to a Photonic Crystal Waveguide. *Phys. Rev. Lett.* **101**, 113903 (2008).
- [10] Makhonin, M. N. *et al.* Waveguide coupled resonance fluorescence from on-chip quantum emitter. *Nano Letters* **14**, 6997–7002 (2014).
- [11] Reithmaier, G. *et al.* On-Chip Generation, Routing, and Detection of Resonance Fluorescence. *Nano Letters* **15**, 5208–5213 (2015).
- [12] Hausmann, B. J. M. *et al.* Integrated Diamond Networks for Quantum Nanophotonics. *Nano Letters* **12**, 1578–1582 (2012).

[13] Sipahigil, A. *et al.* An integrated diamond nanophotonics platform for quantum optical networks. *Science* **354**, 847–850 (2016).

[14] Barclay, P. E., Fu, K. M. C., Santori, C. & Beausoleil, R. G. Chip-based microcavities coupled to nitrogen-vacancy centers in single crystal diamond. *Applied Physics Letters* **95**, 191115 (2009).

[15] Santori, C., Fattal, D., Vucković, J., Solomon, G. S. & Yamamoto, Y. Indistinguishable photons from a single-photon device. *Nature* **419**, 594–597 (2002).

[16] He, Y.-M. *et al.* On-demand semiconductor single-photon source with near-unity indistinguishability. *Nature nanotechnology* **8**, 213–7 (2013).

[17] Somaschi, N. *et al.* Near-optimal single-photon sources in the solid state. *Nat Photon* **10**, 340–345 (2016).

[18] Ding, X. *et al.* On-Demand Single Photons with High Extraction Efficiency and Near-Unity Indistinguishability from a Resonantly Driven Quantum Dot in a Micropillar. *Physical Review Letters* **116**, 020401 (2016).

[19] Kalliakos, S. *et al.* In-plane emission of indistinguishable photons generated by an integrated quantum emitter. *Applied Physics Letters* **104**, 221109 (2014).

[20] Kalliakos, S. *et al.* Enhanced indistinguishability of in-plane single photons by resonance fluorescence on an integrated quantum dot. *Applied Physics Letters* **109**, 151112 (2016).

[21] Dietrich, C. P., Fiore, A., Thompson, M. G., Kamp, M. & Höfling, S. Gaas integrated quantum photonics: Towards compact and multi-functional quantum photonic integrated circuits. *Laser & Photonics Reviews* **10**, 870–894 (2016).

[22] Langbein, W. *et al.* Radiatively limited dephasing in inas quantum dots. *Phys. Rev. B* **70**, 033301 (2004).

[23] Kiraz, A., Atatüre, M. & Imamoğlu, A. Quantum-dot single-photon sources: Prospects for applications in linear optics quantum-information processing. *Phys. Rev. A* **69**, 032305 (2004).

[24] Kiršanské, G. *et al.* Indistinguishable and efficient single photons from a quantum dot in a planar nanobeam waveguide. *arXiv:1701.08131* (2017).

[25] E. Purcell. Spontaneous emission probabilities at radio frequencies. *Phys. Rev.* **69**, 681 (1946).

[26] Englund, D. *et al.* Controlling the Spontaneous Emission Rate of Single Quantum Dots in a Two-Dimensional Photonic Crystal. *Phys. Rev. Lett.* **95**, 13904 (2005).

[27] Akahane, Y., Asano, T., Song, B.-S. & Noda, S. High-Q photonic nanocavity in a two-dimensional photonic crystal. *Nature* **425**, 944–947 (2003).

[28] Painter, O. *et al.* Two-Dimensional Photonic Band-Gap Defect Mode Laser. *Science* **284**, 1819 – 1821 (1999).

[29] Ota, Y. *et al.* Enhanced photon emission and absorption of single quantum dot in resonance with two modes in photonic crystal nanocavity. *Applied Physics Letters* **93**, 183114 (2008).

[30] Kress, A. *et al.* Manipulation of the spontaneous emission dynamics of quantum dots in two-dimensional photonic crystals. *Phys. Rev. B* **71**, 241304 (2005).

[31] Badolato, A. *et al.* Deterministic Coupling of Single Quantum Dots to Single Nanocavity Modes. *Science* **308**, 1158 – 1161 (2005).

[32] Happ, T. D. *et al.* Enhanced light emission of  $In_xGa_{1-x}As$  quantum dots in a two-dimensional photonic-crystal defect microcavity. *Phys. Rev. B* **66**, 41303 (2002).

[33] Kim, J.-H., Cai, T., Richardson, C. J. K., Leavitt, R. P. & Waks, E. Two-photon interference from a bright single-photon source at telecom wavelengths. *Optica* **3**, 577 (2016).

[34] Laurent, S. *et al.* Indistinguishable single photons from a single-quantum dot in a two-dimensional photonic crystal cavity. *Applied Physics Letters* **87**, 163107 (2005).

[35] Coles, R. J. *et al.* Waveguide-coupled photonic crystal cavity for quantum dot spin readout. *Opt. Express* **22**, 2376–2385 (2014).

[36] Bentham, C. *et al.* On-chip electrically controlled routing of photons from a single quantum dot. *Applied Physics Letters* **106**, 221101 (2015).

[37] Gazzano, O. *et al.* Bright solid-state sources of indistinguishable single photons. *Nature communications* **4**, 1425 (2013).

[38] Reithmaier, G. *et al.* A carrier relaxation bottleneck probed in single inGaAs quantum dots using integrated superconducting single photon detectors. *Applied Physics Letters* **105**, 081107 (2014).

[39] Zibik, E. A. *et al.* Long lifetimes of quantum-dot intersublevel transitions in the terahertz range. *Nature Materials* **8**, 803–807 (2009).

[40] Urayama, J., Norris, T. B., Singh, J. & Bhattacharya, P. Observation of phonon bottleneck in quantum dot electronic relaxation. *Physical Review Letters* **86**, 4930–4933 (2001).

[41] Berstermann, T. *et al.* Systematic study of carrier correlations in the electron-hole recombination dynamics of quantum dots. *Physical Review B* **76**, 165318 (2007).

[42] Stievater, T. H. *et al.* Rabi oscillations of excitons in single quantum dots. *Phys. Rev. Lett.* **87**, 133603 (2001).

[43] Zrenner, A. *et al.* Coherent properties of a two-level system based on a quantum-dot photodiode. *Nature* **418**, 612–614 (2002).

[44] Ramsay, A. J. *et al.* Phonon-Induced Rabi-Frequency Renormalization of Optically Driven Single InGaAs/GaAs Quantum Dots. *Physical Review Letters* **105**, 177402 (2010).

[45] Giesz, V. *et al.* Coherent manipulation of a solid-state artificial atom with few photons. *Nature Communications* **7**, 11986 (2016).

[46] Melloni, A. *et al.* Tunable delay lines in silicon photonics: Coupled resonators and photonic crystals, a comparison. *IEEE Photonics Journal* **2**, 181–194 (2010).

[47] Englund, D. *et al.* Ultrafast photon-photon interaction in a strongly coupled quantum dot-cavity system. *Phys. Rev. Lett.* **108**, 093604 (2012).

[48] Loo, V. *et al.* Optical nonlinearity for few-photon pulses on a quantum dot-pillar cavity device. *Phys. Rev. Lett.* **109**, 166806 (2012).

[49] Nguyen, H. S. *et al.* Ultra-coherent single photon source. *Applied Physics Letters* **99**, 261904 (2011).

[50] Matthiesen, C., Vamivakas, A. N. & Atatüre, M. Subnatural linewidth single photons from a quantum dot. *Physical Review Letters* **108**, 093602 (2012).

[51] Proux, R. *et al.* Measuring the photon coalescence time window in the continuous-wave regime for resonantly driven semiconductor quantum dots. *Physical Review Letters* **114**, 067401 (2015).

[52] Bennett, A. J. *et al.* Cavity-enhanced coherent light scattering from a quantum dot. *Science Advances* (2016).

[53] Konthasinghe, K. *et al.* Coherent versus incoherent light scattering from a quantum dot. *Phys. Rev. B* **85**, 235315

(2012).

[54] Duan, L.-M. & Raussendorf, R. Efficient quantum computation with probabilistic quantum gates. *Phys. Rev. Lett.* **95**, 080503 (2005).

[55] Duan, L.-M. *et al.* Probabilistic quantum gates between remote atoms through interference of optical frequency qubits. *Phys. Rev. A* **73**, 062324 (2006).

[56] Cabrillo, C., Cirac, J. I., García-Fernández, P. & Zoller, P. Creation of entangled states of distant atoms by interference. *Phys. Rev. A* **59**, 1025–1033 (1999).

[57] Stockill, R. *et al.* Phase-tuned entangled state generation between distant spin qubits. *arXiv:1702.03422* (2017).

[58] Matthiesen, C. *et al.* Phase-locked indistinguishable photons with synthesized waveforms from a solid-state source. *Nature Communications* **4**, 1600 (2013).

[59] Reigue, A. *et al.* Probing electron-phonon interaction through two-photon interference in resonantly driven semiconductor quantum dots. *ArXiv:1612.07121* (2016).

[60] Thoma, A. *et al.* Exploring dephasing of a solid-state quantum emitter via time- and temperature-dependent hong-ou-mandel experiments. *Phys. Rev. Lett.* **116**, 033601 (2016).

[61] Loredo, J. C. *et al.* Scalable performance in solid-state single-photon sources. *Optica* **3**, 433–440 (2016).

[62] Iles-Smith, J., McCutcheon, D. P. S., Nazir, A. & Mørk, J. Phonon limit to simultaneous near-unity efficiency and indistinguishability in semiconductor single photon sources. *ArXiv:1612.04173* (2016).

[63] Fan, S., Kocabas, E. & Shen, J.-T. Input-output formalism for few-photon transport in one-dimensional nanophotonic waveguides coupled to a qubit. *Phys. Rev. A* **82**, 063821 (2010).

[64] Lindner, N. H. & Rudolph, T. Proposal for pulsed on-demand sources of photonic cluster state strings. *Phys. Rev. Lett.* **103**, 113602 (2009).

[65] Schwartz, I. *et al.* Deterministic generation of a cluster state of entangled photons. *Science* **354**, 434–437 (2016).

# Supplementary Materials: High Purcell factor generation of coherent on-chip single photons

## CAVITY-WAVEGUIDE COUPLING EFFICIENCY

The coupling efficiency  $\beta$  between the M1 mode and the waveguides can be estimated according to  $\beta = 1 - Q_{\text{M1}}/Q_{\text{u}}$  (Coles et al., Optics Express, 22, 3, 2014), where  $Q_{\text{M1}}$  (540) denotes the  $Q$  factor of the M1 mode;  $Q_{\text{u}}$  (1109) is the measured average  $Q$  factor of cavities fabricated without waveguides on the same sample. The total coupling efficiency between the M1 mode and the two waveguides is therefore  $\beta = 51\%$ . The coupling efficiency for each waveguide (see Fig. 1(b)) is 41% and 10% respectively, estimated from the ratio (4:1) of the QD PL intensity measured from the two out-couplers when the QD is resonant with M1. FDTD simulations (Coles et al., Optics Express, 22, 3 2014) show that a maximum theoretical coupling efficiency of up to 89 % between the cavity mode and the waveguide could be achieved in an optimized device.

## EXCITON FINE-STRUCTURE SPLITTING AND EIGENSTATE ORIENTATION

The charge species of the studied exciton is identified by measuring the exciton fine-structure splitting (FSS). Fig. S1 shows the peak energy of the QD emission as a function of the angle ( $\theta$ ) of the detected polarization. A FSS of  $19 \mu\text{eV}$  is clearly observed, illustrating that the exciton under study is a neutral exciton.

The inset shows high power PL spectra of the two cavity modes measured when the polarizer is co-polarized with the M1 (blue line,  $\theta = 168^\circ$ ) and M2 (orange line,  $\theta = 258^\circ$ ). Note that the two QD eigenstates are co-polarized with the two cavity modes respectively, which is expected since both the QD eigenstates and the fundamental modes of the H1 PhCC were intended to be aligned parallel/perpendicular to the (110) crystal axes.

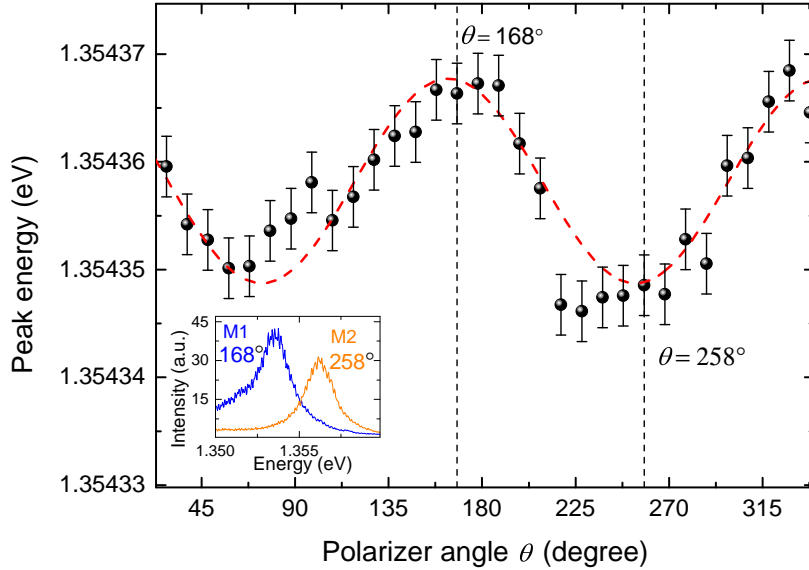


FIG. S1. Peak energy of the QD emission versus the angle ( $\theta$ ) of the detected polarization. Red dashed lines: guide for the eye. Inset: PL spectra of the two cavity modes measured when the polarizer is co-polarized with mode M1 (blue line), and mode M2 (orange line).

## DIPOLE COUPLING STRENGTH, POSITION AND ORIENTATION

At zero QD-cavity detuning and for perfect dipole positioning and orientation, the Purcell factor is

$$F_{\text{P}} = \frac{3}{4\pi^2} \frac{Q}{V_m} = \frac{2g^2}{\kappa\gamma} = 2C, \quad (\text{S1})$$

where  $Q$  is the quality factor,  $V_m$  the mode volume in cubic wavelengths  $(\lambda/n)^3$ ,  $\hbar g$  the QD-cavity coupling strength ( $\mu\text{eV}$ ),  $2\hbar\kappa$  the cavity linewidth ( $\mu\text{eV}$ ),  $\hbar\gamma$  the QD's natural linewidth ( $\mu\text{eV}$ ), and  $C$  the cooperativity.  $Q$  (and  $\kappa$ ) are known from a high-power PL measurement, and  $V_m$  is taken from FDTD simulations approximating the real fabricated system rather than the ideal H1 value (giving 0.63 rather than 0.39  $(\lambda/n)^3$ ). These  $Q$  and  $V_m$  values give the ideal  $F_P$  for the fabricated cavity as 65. Then, using the ensemble lifetime  $T'_1$  of QDs outside the cavity to obtain  $\gamma = 1/T'_1$ ,  $\hbar g$  is calculated to be 169  $\mu\text{eV}$  for the ideal  $F_P$  (i.e. for ideal coupling), and 135  $\mu\text{eV}$  for the measured QD-cavity system with  $F_P = 42$ , through (Khitrova et al., Nat. Phys. 2, 81-90, 2006):

$$g = \sqrt{\frac{\omega |\vec{\epsilon}(\vec{r}_0) \cdot \vec{\mu}|^2}{2\hbar\varepsilon_0 n^2 V_m}}, \quad (\text{S2})$$

and

$$|\vec{\mu}| = \sqrt{3\pi\hbar\varepsilon_0 \frac{\gamma c^3}{n\omega^3}}. \quad (\text{S3})$$

The calculated QD dipole moment from eq. S3 is  $|\vec{\mu}| = 27.6$  D.  $\vec{\epsilon}(\vec{r}_0)$  is the field at the QD position normalized to the cavity field maximum  $\vec{E}(\vec{r}_0)/\vec{E}_{\max}$ . Then, knowing that for the measured Purcell factor we have  $\hbar g = 135 \mu\text{eV}$ , where the maximum is 169  $\mu\text{eV}$ , it follows that  $|\vec{\epsilon}(\vec{r}_0) \cdot \vec{\mu}|^2 / |\vec{\mu}|^2 = 0.8^2$ , i.e. the spatial overlap and alignment of the QD dipole and the cavity mode is  $\sim 80\%$  ideal. The high coupling is shown by both the very short lifetime and the very large Mollow splitting, discussed in section . The large cavity loss does however prevent the system entering the strong-coupling regime, i.e. vacuum Rabi-splitting. This occurs when (Reithmaier et al., Nature 432, 197-200, 2004):

$$16g^2 > (2\kappa - \gamma)^2, \quad (\text{S4})$$

a condition not satisfied for this  $g$  and  $\gamma$  until  $Q > 3200$  and  $F_P \sim 250$ . The system thus remains in the weak coupling regime despite the large coupling strength. In general we want  $\kappa/2 > g \gg \gamma$  in order to obtain a highly coherent on-chip single-photon source. The device we report here has  $\hbar\{2\kappa, g, \gamma\} = \{2510, 135, 0.7\} \mu\text{eV}$ .

## INFLUENCE OF THE CAVITY ON EXCITATION EFFICIENCY

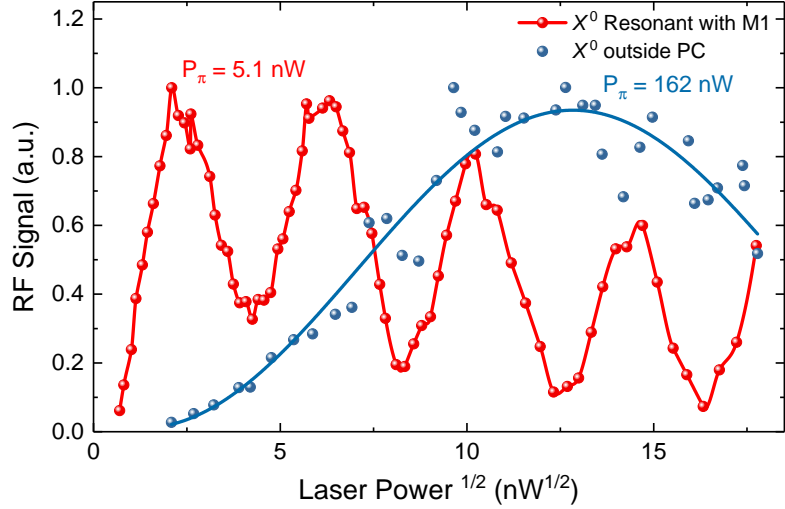


FIG. S2. Comparison between Rabi rotation data for the QD exciton resonant with the M1 cavity mode (red data) and a different QD exciton located outside the photonic crystal (blue data). It can be seen that the cavity acts to strongly enhance the electric field experienced by the QD, reducing the power required for a  $\pi$ -pulse by approximately a factor of 32.

Owing to the localized optical field enhancement, the cavity should also serve to strongly enhance the excitation efficiency by reducing the amount of laser power to reach population inversion (a  $\pi$ -pulse). To confirm this, we compare a Rabi rotation measured using the QD-cavity system studied in the main text to one measured on the neutral exciton of a different QD which is on the same sample but outside the photonic crystal. This is shown in Fig. S2. A decrease in  $\pi$ -pulse power of approximately 32 is found for the QD in the cavity, confirming this hypothesis. As expected, increasing  $\pi$ -power as a function of QD-cavity detuning was also observed when calibrating the pulse areas ( $\Theta$ ) for detuned DPRF measurements. The resonant  $\pi$ -power of 5.1 nW (corresponding to a pulse energy of 67 aJ) illustrates the low optical power requirements of the source compared to parametric down-conversion (PDC) sources, which typically are driven with mW powers.

## RESONANT RAYLEIGH SCATTERING

Resonant Rayleigh scattering (RRS) refers to coherent scattering of single laser photons by a two-level system, in this case the QD exciton (e.g. Matthiesen et al., Phys. Rev. Lett. 108, 093602, 2012). This section presents some additional details to support the data presented in Fig. 3 of the main text.

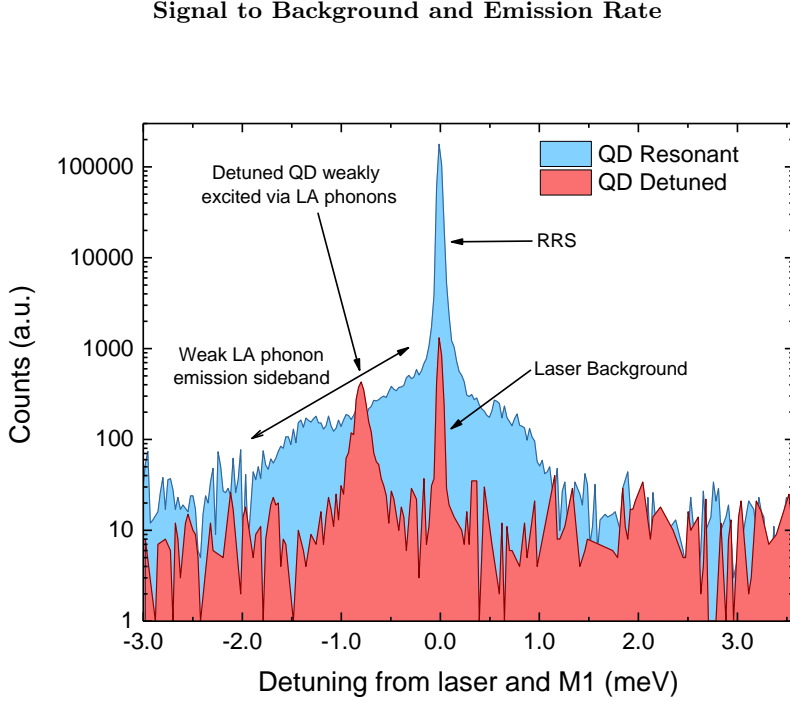


FIG. S3. Log-linear spectrum of the device under weak resonant CW excitation (25 nW,  $\Omega_R/2\pi \simeq 2$  GHz) when the QD is either resonant (blue data) or detuned (red data, detuning  $-0.77$  meV) from the laser and M1 cavity mode. The cavity excitation / waveguide collection scheme used for the correlation measurements was used here. As this spectrum was taken with a spectrometer and CCD as opposed to the FPI, it is not possible to resolve the RRS and RF components as they are both resolution-limited by the instrument.

To determine the signal to background ratio in the RRS measurements, we compare spectra (taken with the spectrometer and CCD) with the QD resonant with and detuned from the laser, similar to the method shown for pulsed driving in Fig. 1(c) of the main text. The laser suppression is considerably stronger for the single mode CW laser as the narrow spectral width reduces the influence of birefringence in the optical setup. As a result, it is necessary to plot the intensity on a logarithmic scale for the laser background peak to be visible. This is shown for the case of cavity excitation and waveguide collection at a driving power of 25 nW ( $\Omega_R/2\pi \simeq 2$  GHz) in Fig. S3. In the Fabry-Pérot measurements in the main text, an RRS fraction of 87.4 % was found at this drive strength.

Comparison of the areas of the central peaks gives a signal to background ratio (SBR) of approximately 150:1. The absence of a significant peak at the detuning  $\Delta = 0$  (where  $\Delta$  is the detuning relative to the laser and M1 cavity mode) in the QD detuned spectrum demonstrates the fundamental role that interaction between the emitter and laser plays in coherent scattering. When the QD is resonant, weak asymmetric sidebands corresponding to emission ( $\Delta < 0$ ) or absorption ( $\Delta > 0$ ) of a longitudinal acoustic (LA) phonon followed by spontaneous emission of a photon can be observed. It is also notable that in the detuned case a small amount of spontaneous emission from the zero-phonon line (ZPL) is still observed as the QD is weakly (owing to very small  $\Omega_R$ ) excited via LA phonon emission (Quilter et al., Phys. Rev. Lett. 114, 137401, 2015).

In order to determine the count-rate in the waveguide in this regime where RRS is dominant, we measure the count-rate under the same conditions as the resonant data measured in Fig. S3. To do this, a single SPAD is connected directly to the collection fibre, and a count-rate of  $66.0 \pm 0.8$  kHz is measured. Using FDTD simulations, the first lens is found to collect 14 % of the light scattered by the out-coupler with 23 % of this coupled into the single mode collection fibre. The beamsplitter in the setup also causes a loss of 50 % whilst the linear polarizer has a transmission

of 84 % for a perfectly co-polarized input. Finally, the SPAD has a quantum efficiency of 43 % at the QD wavelength. Combining these losses, a collection efficiency of 0.58 % is deduced, leading to an estimated waveguide count-rate of  $11.5 \pm 0.4$  MHz at this high RRS fraction.

### Analysis of the Fabry-Pérot spectra

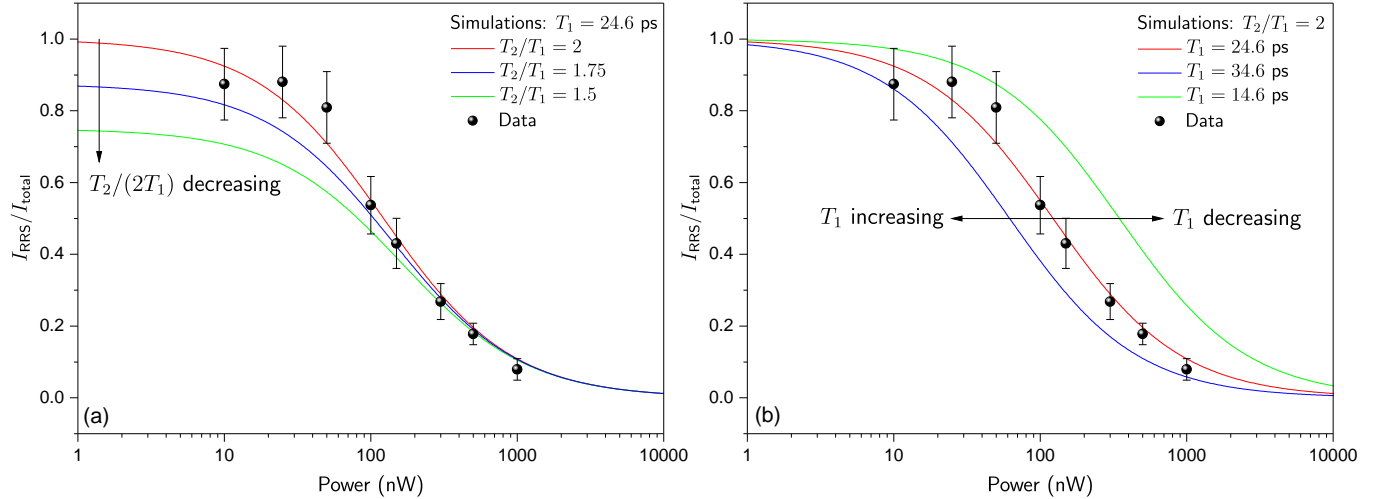


FIG. S4. Experimental  $I_{\text{RRS}}/I_{\text{total}}$  (black spheres) and fits with Eq. 3 from the main text (coloured lines). (a) Illustration of the effect of reduced coherence. Here the curves have the same  $T_1$  value, and together they show that a high fraction of coherent scatter at low power implies that the emitter coherence is very close to the radiative limit. For  $T_2/T_1 = 1.5$  (green curve), for example, it is not possible to reach 80 %  $I_{\text{RRS}}$ . (b) Illustration of the effect of varying  $T_1$ . Comparing radiatively-limited curves ( $T_2 = 2T_1$ ), we see that the point at which coherent scattering gives way to incoherent scattering is strongly dependent on  $T_1$ . This is a reflection of the fact that shorter lifetimes have higher saturation powers. For both (a) and (b) the red curve is the fit shown in Fig. 3 of the main text.

This section provides further information on how the data for Fig. 3 was obtained. The Fabry-Pérot spectra consisted of a series of peaks separated by the free spectral range (FSR). These have three components: RRS, SE, and laser background. At low power the laser background, observed by detuning the dot, is negligible (0.5 % for 10 nW). This background increases with power and is in all cases subtracted. A function consisting of the sum of a Lorentzian peak (for the SE) and a Gaussian peak (for the RRS) was fitted to the data. Here the Gaussian was used to approximate the Fabry-Pérot instrument response function (IRF), from which the sub-IRF linewidth coherent scatter cannot be distinguished. At low powers the SE component is spectrally broad with negligible intensity, and the fits are therefore constrained using a linewidth obtained from higher power measurements. The 500 nW and 1000 nW SE components were adjusted to account for clipping of the signal as the Mollow side peaks approach the edge of the filtering window.

Figure 3 in the main text shows that the  $I_{\text{RRS}}/I_{\text{total}}$  data is well reproduced by a fit of Equation 2 that results in values of  $T_1 = (24.6 \pm 1.6)$  ps and  $T_2/(2T_1) \sim 1$ . Fig. S4 shows that the theoretical curve is very sensitive to the values of both these quantities. The high fractions of RRS ( $\sim 87$  %) observed at low power are only possible if  $T_2/(2T_1) \sim 1$  (Fig. S4(a)), and  $T_1$  determines the point at which incoherent scattering begins to dominate. With  $T_1 = 14.6$  or 34.6 ps this occurs much too late or early respectively (Fig. S4(b)), showing the high sensitivity to  $T_1$ , and providing additional confirmation of the value of  $T_1$  deduced from the DRPF measurements.

### Mollow triplet and Rabi frequencies

As discussed in the main text, when  $\Omega_R \ll 1/T_1$  we observe RRS. At high driving strengths the fraction of RRS reduces and eventually a Mollow triplet forms, as shown in Fig. S5(a). This occurs when the damped Rabi frequency  $\Omega_R^d$ , given by (Muller et al., Phys. Rev. Lett. 99, 187402, 2007)

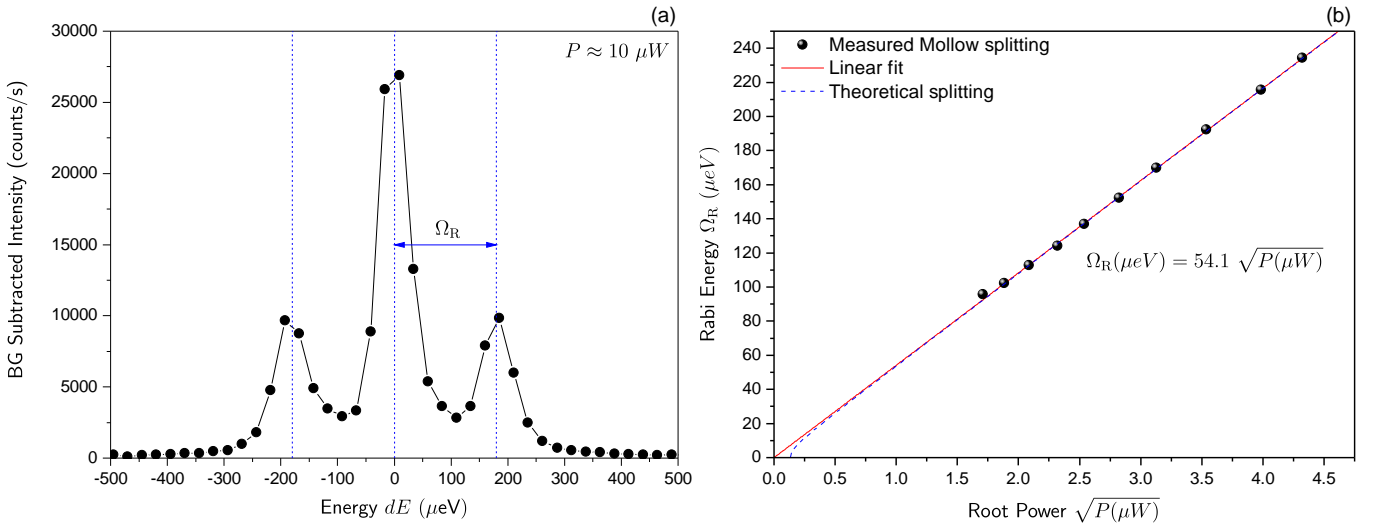


FIG. S5. (a) A high power ( $\sim 10 \mu\text{W}$ ) background-subtracted spectrum showing the very large Mollow splitting. (b) The measured dependence of the splitting on laser power and the deduced theoretical splitting from eq. S5. At very low powers the splitting is damped and no triplet occurs.

$$\Omega_R^d = \sqrt{\Omega_R^2 - \frac{1}{4} \left( \frac{1}{T_1} - \frac{1}{T_2} \right)^2}, \quad (\text{S5})$$

becomes real. The splitting is proportional to the square root of the power and allows us to extrapolate the Rabi frequency down to the low powers of the RRS regime, as shown in Fig. S5(b).

## MASTER EQUATION SIMULATIONS

A Lindblad master equation (ME) for two-level system (2LS) cavity QED with coherent driving of the cavity mode is (Carmichael, Statistical Methods in Quantum Optics 2: Non-classical fields, Springer, 2008):

$$\begin{aligned} \dot{\rho} = & -\frac{i}{2}\omega_A[\sigma_z, \rho] - i\omega_C[a^\dagger a, \rho] \\ & + g[a^\dagger \sigma_- - a\sigma_+, \rho] - i[\bar{E}_0 e^{-i\omega_0 t} a^\dagger + \bar{E}_0^* e^{i\omega_0 t} a, \rho] \\ & + \frac{\gamma}{2}(2\sigma_- \rho \sigma_+ - \sigma_+ \sigma_- \rho - \rho \sigma_+ \sigma_-) + \kappa(2a\rho a^\dagger - a^\dagger a \rho - \rho a^\dagger a), \end{aligned} \quad (\text{S6})$$

where  $g$ ,  $\kappa$  and  $\gamma$  are defined in Section ,  $\omega_A$  and  $\omega_C$  are the frequencies of the 2LS and cavity respectively,  $\bar{E}_0$  and  $\omega_0$  are the amplitude and frequency of the driving field, and  $\hbar = 1$ . In this section it is used as a basis to:

- A. Compare the SPAD lifetime measurements to the DPRF and RRS measurements.
- B. Explain the discrepancy between resonant and non-resonant PL decay rates.
- C. Analyze the principle, the results, and the implications of the DPRF technique.

The ME was solved and analyzed with the help of QuTiP, the Quantum Toolbox in Python (Johansson et al., Comp. Phys. Comm. 184, 1234, 2013). The pulses were modelled as Gaussians with electric-field FWHM  $\tau_L$ .

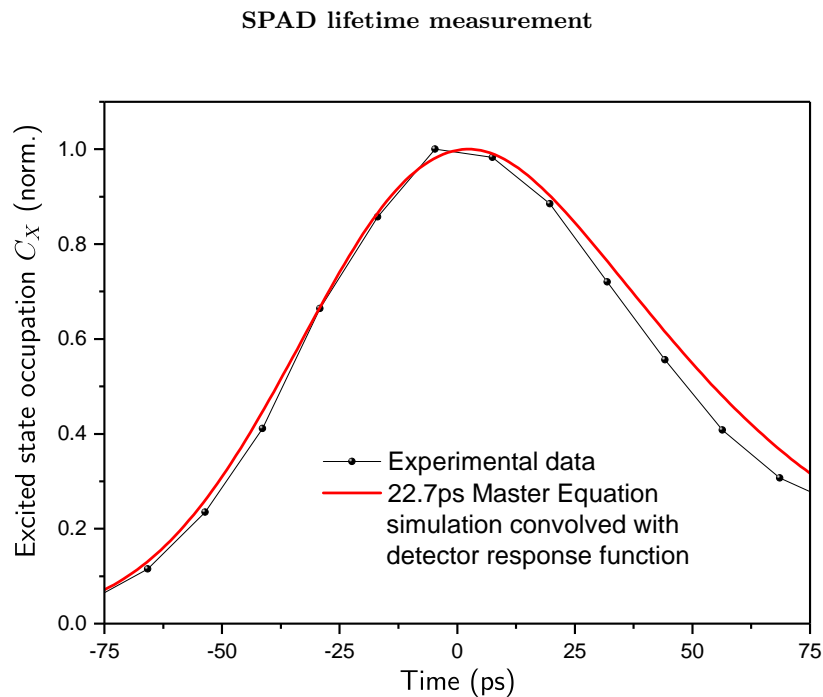


FIG. S6. Comparison of the lifetime measured with a SPAD (FWHM  $\sim 60$  ps) to a simulation of the 22.7 ps decay under  $\pi$ -pulse excitation, after convolving the simulation with a measured detector response function.

The SPAD lifetime measurements described in the main text revealed that the exciton lifetime was too short to reliably measure with the instrument time response FWHM ( $\sim 60$  ps). Nevertheless, once the lifetime was known via other techniques (DPRF and RRS), it was possible to simulate the pulsed population dynamics with the ME, convolve this with the IRF, and compare with the data. The results of this procedure are shown in Fig. S6. The agreement is very good, and the small discrepancy is believed to be due to variabilities in the IRF, which changes with wavelength and focus on the SPAD. These changes become significant when operating at or below the quoted limit of the detector. Nevertheless the SPAD measurements further justify the DPRF result and the lifetime extracted from the RRS.

### Comparison of resonant and non-resonant excitation decay dynamics

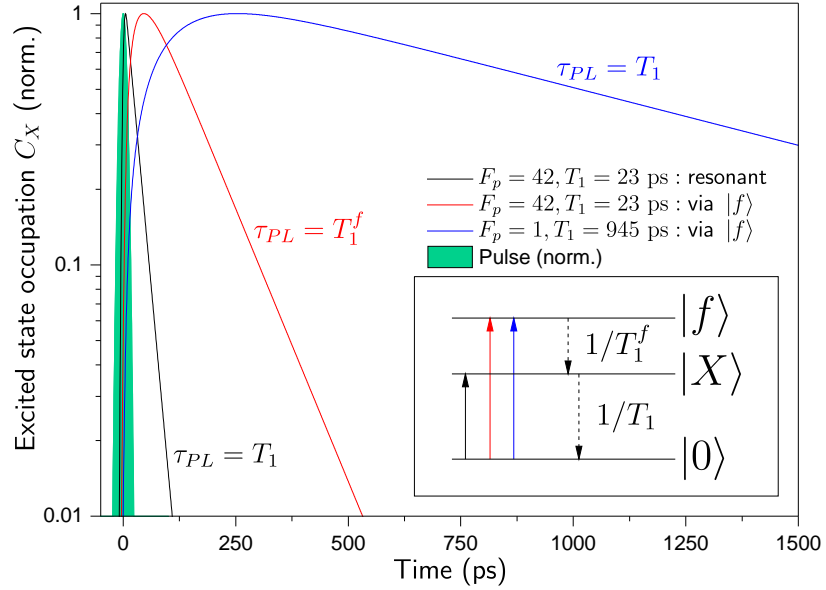


FIG. S7.  $|X\rangle$  population dynamics under various excitation conditions. When exciting resonantly (black curve), a fast rise and decay at the Purcell-enhanced rate (here  $T_1 = 23$  ps with  $F_p = 42$ ) is observed. For excitation via a higher energy state  $|f\rangle$  which populates  $|X\rangle$  at a rate  $1/T_1^f$ , with  $T_1^f = 100$  ps (red curve), we see a slower rise and a decay rate of 100 ps, i.e. the decay rate in this case is determined by the slow filling rate of the state. If we turn off the Purcell enhancement to make the  $|X\rangle$  decay rate 945 ps, and again fill the state via the now relatively fast decaying third higher level (blue curve), we see a very slow rise but what we measure at long times is again the true  $|X\rangle$  decay rate of 945 ps. Inset: Energy level diagram.

The effect on the time-resolved  $|X\rangle$  dynamics when exciting via a third higher energy state  $|f\rangle$  is shown in Fig. S7. An additional collapse operator has been added to the ME to allow  $|f\rangle \rightarrow |X\rangle$  decay at a rate  $1/T_1^f$ , where  $T_1^f$  is the lifetime of the higher state. With resonant pulses (exciting  $|0\rangle \rightarrow |X\rangle$  directly via the cavity mode), a fast rise and decay at the Purcell-enhanced rate is observed. When exciting  $|X\rangle$  via  $|0\rangle \rightarrow |f\rangle$  with  $T_1^f > T_1$ , the observed decay rate of the  $|X\rangle$  population  $\tau_{PL}$  is determined by the filling rate of the state,  $1/T_1^f$ , rather than the Purcell-enhanced decay rate  $1/T_1$ . For  $T_1^f \ll T_1$ , the time-resolved PL curve approaches the resonant case. Thus, a time-resolved pulsed PL measurement will determine the radiative transition rate and hence Purcell factor only when the radiative rate is the slowest process in the excitation-emission cycle. This explains the observed difference in the time-resolved PL decay observed under above-barrier and resonant excitation shown in Fig. 1(d), in the case of slow carrier relaxation.

### DPRF

The principle of the double  $\pi$ -pulse resonance fluorescence (DPRF) technique is illustrated in Fig. S8 via ME simulations of the time dynamics of the excited state  $|X\rangle$  for several inter-pulse separations. These separations are indicated by red dots in Fig. S9, which shows the expected counts and photon number distributions.

The main features of DPRF are determined by the emitter time-constant  $T_1 = 1/(\gamma F_p)$ , the pulse-width  $\tau_L$ , and the ratio of the two. The maximum instantaneous population inversion due to a single  $\pi$ -pulse is proportional to  $T_1/\tau_L$ . Thus the maximum depopulation due to the second  $\pi$ -pulse is also proportional to  $T_1/\tau_L$ , and the point at which this occurs is determined by  $\tau_L$ , since at  $\Delta\tau = 0$  the pulses combine to give a  $\sqrt{2}\pi$ -pulse. However, upon separation of the pulses, the recovery of the signal is determined only by  $T_1$ . As such, one can obtain the emitter lifetime even with  $\tau_L > T_1$  provided one fits away from the region where the pulses overlap temporally. Experimentally, some additional noise may be seen around  $\Delta t = 0$  due to interference between the pulses as they are combined in the optical setup.

The solutions to the ME thus far have used the density matrix formalism and thus produced expectation values for ensemble averages. Now the Monte-Carlo method is employed to gain insight into the composition of these averages. In particular we are interested in the number of quantum jumps from the  $|X\rangle$  state to the ground state over the

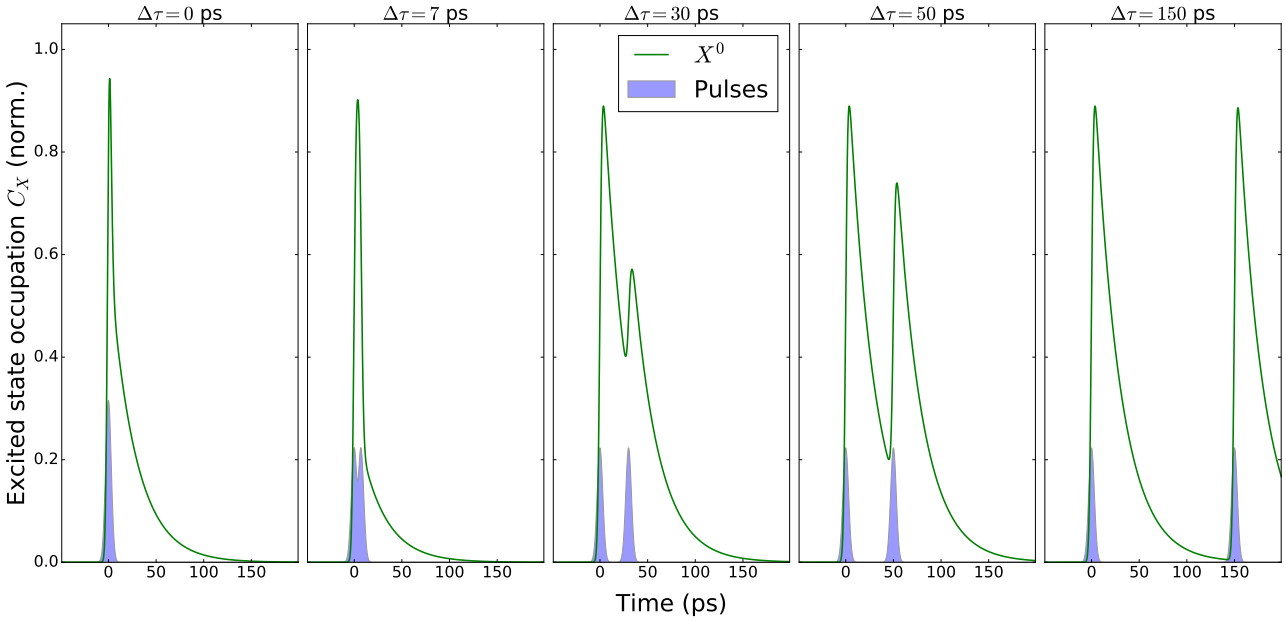


FIG. S8. The principle of the DPRF method shown via ME simulations of the system with two 7 ps  $\pi$ -pulses. The total occupation probability is minimum around  $\Delta t = 7$  ps when the pulses just separate and can effectively populate and depopulate the state. The total population recovers exponentially with a time-constant given by the emitter lifetime.

entire course of the two  $\pi$ -pulse system evolution for a single run of the system – a single quantum trajectory. By counting the jumps of thousands of such trajectories we obtain a probability distribution for the number of quantum jumps, and therefore the number of emissions – with some probability  $P[0]$  we will get 0 photons after two  $\pi$ -pulses, some probability  $P[1]$  we will get 1 photon etc. This is repeated for different inter-pulse separations. Fig. S9 shows the photon number probabilities for different pulse separations (blue) and the average total number of photons per trajectory (black). Close to  $\Delta\tau = 0$ , 0-photon events dominate, and for  $\Delta\tau \gg 0$ , 2-photon events are the most probable. Except very close to zero, 1-photon events are very improbable – showing that in general the  $\pi$ -pulses either both create a photon each or else cancel each other out. For the simulated pulse-length ( $\tau_L \sim T_1/4$ ) there is a small probability of multi-photon emission for each  $\pi$ -pulse, and so the expected count is slightly larger than 2 for large pulse separations.

The double pulse simulations also highlight a point concerning photon number purity. As the dashed blue line in Fig. S9 shows, 2-photon purity increases with  $\pi$ -pulse separation on a time scale determined by the emitter lifetime. For negligibly short pulses

$$P[2] = 1 - e^{-\frac{\Delta\tau}{\tau_L}}. \quad (\text{S7})$$

For  $\Delta\tau = 5T_1$  the 2-photon purity is 99.3 %. By extension, very high photon-number fidelity per pulse under  $N$  sequential  $\pi$ -pulses requires separations much longer than the emitter time constant. This therefore puts a stronger requirement on emitter lifetime for high  $\pi$ -pulse repetition rates.

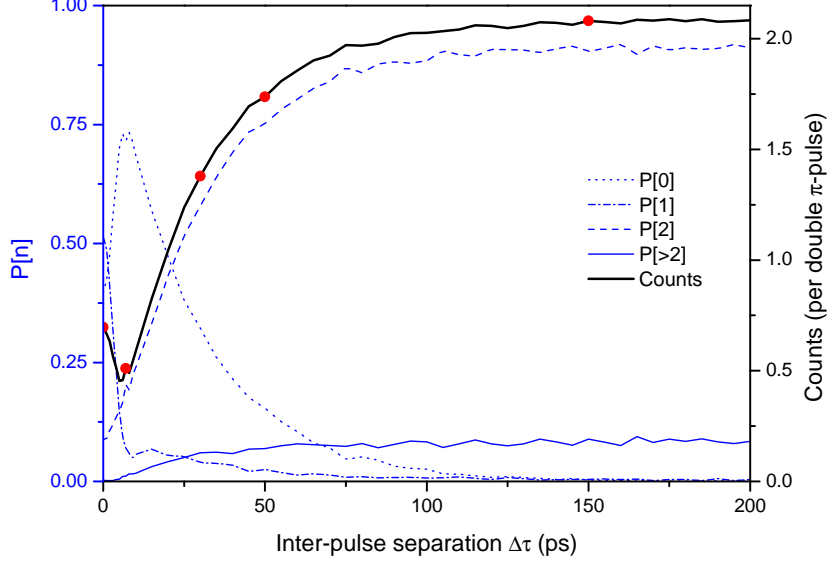


FIG. S9. Monte-Carlo simulations of the DPRF technique. The black curve shows the expected counts, and the blue curves show the composition of the expected counts in terms of photon number distributions. The simulations reveal that the expected signal recovers on the timescale of the emitter lifetime. The red points refer to the pulse separations depicted in Fig. S8.

### CORRELATION MEASUREMENTS

The Hanbury-Brown-Twiss (HBT) and Hong-Ou-Mandel (HOM) measurements are performed using a pair of single photon avalanche photodiodes (SPADs) selected for maximum quantum efficiency ( $\sim 43\%$ ) at the cavity wavelength of  $\sim 915$  nm. The combined instrument response function (IRF) of the two detectors when used with the photon counting card (TCSPCM) is Gaussian in shape with a FWHM of  $\sim 860$  ps. The photon counting card is configured with a 100 ns delay window, corresponding to a time bin width of 97.7 ps. A fixed electrical delay of 50 ns is added to one SPAD to centre the time-zero peak in the window.

For the HBT measurement the collection fibre of the setup is fed straight to a fibre splitter with a SPAD on each output. For the HOM measurement a fibre interferometer is used in the Mach Zehnder configuration as illustrated in Fig. S10(a). Fibre paddles are used to correct for birefringence induced by the fibres, ensuring polarization matching at the second fibre splitter where photon coalescence occurs. A short delay fibre is added to one arm to introduce a delay of 2 ns with respect to the other. The delay time is chosen to be significantly larger than both the emitter lifetime and detector response time, ensuring well-resolved peaks. A motorized half-wave plate (HWP) allows the polarization of the other arm to be rotated between co- and cross-polarized with respect to the other, making the photons either maximally or minimally distinguishable. The waveplate is rotated between every 15 minute acquisition cycle to minimize the influence of any time-dependent drifts.

A characteristic series of 5 peaks is observed centered around zero time delay (Santori et al., *Nature* 419, 594-597, 2002) as shown in Fig. S10(b). We denote the areas of these peaks as  $A_n$ , numbered from left to right (see Fig. S10(b)). As the detector IRF ( $\sim 860$  ps) is much greater than the QD lifetime (22.7 ps), the peaks can be well-fitted using Gaussian functions with the width of the detector response as shown in Fig. S10(b). This contrasts to the typical case of small Purcell enhancement where the IRF and QD lifetime are similar and it is necessary to convolve the IRF with the exponential QD response. At zero delay on the TCSPCM, single photons from subsequent pulses interfere. Comparing the areas of this peak for the co- and cross-polarized cases allows extraction of the raw visibility according to eq. S8:

$$V = \frac{A_{3\perp} - A_{3\parallel}}{A_{3\perp}}. \quad (\text{S8})$$

To extract the true visibility of the two-photon interference, it is necessary to correct for both the multi-photon emission of the source ( $g^{(2)}(0)$ ) and deviations of the interferometer beamsplitter from ideal behavior. The relevant

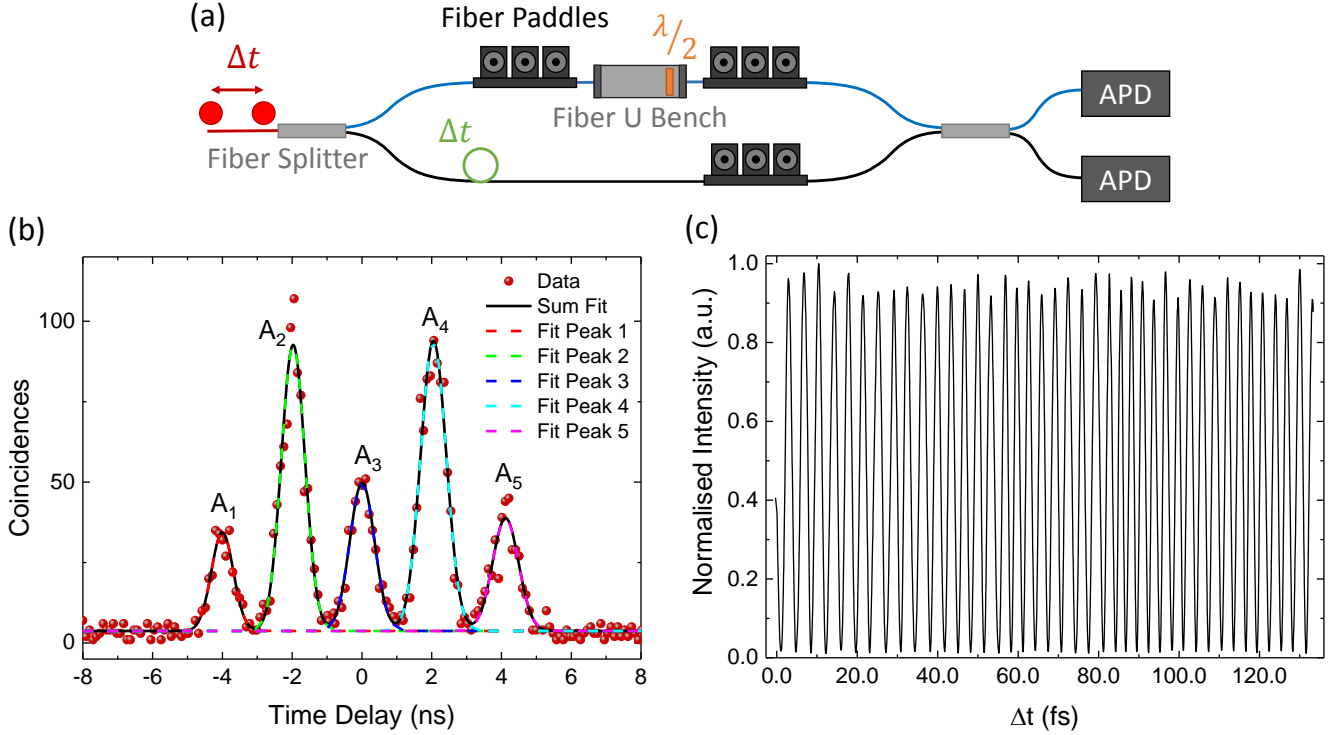


FIG. S10. (a) Schematic of the Mach-Zehnder interferometer used for the HOM measurements. (b) Coincidence count data for the co-polarized (||) case. The dashed lines show the individual Gaussian (with width from the SPAD IRF) fits to each peak whilst the black line shows the cumulative fit. (c) Interference fringes measured by piezo tuning the path length of one interferometer arm. A single mode laser at the wavelength of the M1 mode is used and the interferometer is configured to be co-polarized with equal arm lengths. The transmission is monitored using a single detector on one output port of the interferometer.

parameters are  $g_{HBT}^{(2)}(0)$ , the interferometer fringe contrast  $(1 - \epsilon)$  and the beam-splitter reflection and transmission coefficients ( $R, T$ ). These parameters for our experiment are given in Table S1. The fringe contrast was measured by adding a piezo-tunable air-gap to one arm of the interferometer, equalizing the length of the two arms and measuring the transmission of a single mode laser (at the wavelength of the M1 mode) through the interferometer in the co-polarized configuration as a function of this delay. The raw data of this measurement is shown in Fig. S10(c). The value in Table S1 was obtained by finding the fringe contrast  $(= (I_{max} - I_{min}) / (I_{max} + I_{min}))$  for each fringe and taking the mean.

Parameter	Value	Correction	Measurement Method
$(1 - \epsilon)$	$0.968 \pm 0.004$	6.38 %	Fringe contrast measurement with single mode laser
$g_{HBT}^{(2)}(0)$	$0.134 \pm 0.003$	19.5 %	HBT measurement
$R$	$0.544 \pm 0.002$	1.53 %	Resonant transmission with single mode laser
$T$	$0.456 \pm 0.002$		
Polarisation	$99.99 \pm 0.01\%$	0	Resonant extinction with single mode laser

TABLE S1. Parameters used in the correction of the two-photon interference visibility. The contribution of each to the corrected value is estimated in the correction column. These values are approximate owing to the co-dependence of parameters in eqs. S9 and S10.

The influence of these values is shown in eq. S9 by their effect on the amplitude of the central peak in the HOM measurement (Santori et al., Nature 419, 594-597, 2002):

$$A_3 \propto (R^3 T + R T^3)(1 + 2g^{(2)}(0)) - 2(1 - \epsilon)^2 R^2 T^2 V. \quad (S9)$$

By taking  $V = 1$  for  $A_{3\parallel}$  and  $V = 0$  for  $A_{3\perp}$  we can evaluate the raw visibility that would be measured for perfectly

indistinguishable photons under these conditions. Our measured raw visibility can then be normalized by this to obtain the corrected value. Equivalently, it is also possible to perform the correction using a single formula that compares  $A_{3\parallel}$  to  $A_{2\parallel}$  and  $A_{4\parallel}$  (eq. S10) (Somaschi et al., Nat. Photon., 10, 340-345, 2016):

$$V = \frac{1}{(1-\epsilon)^2} \left[ 2g^{(2)}(0) + \frac{R^2 + T^2}{2RT} - \frac{A_{3\parallel}}{A_{2\parallel} + A_{4\parallel}} \left( 2 + g^{(2)}(0) \frac{(R^2 + T^2)}{RT} \right) \right]. \quad (\text{S10})$$

Using the values from table S1, eq. S9 yields a corrected visibility of  $V = 79.6 \pm 5.9$  % whilst eq. S10 gives  $V = 79.8 \pm 5.7$  %. The dominant term in this correction is the non-unity purity of the emission characterised by  $g_{HBT}^{(2)}(0)$ . The presence of laser background is not corrected for in this approach (other than the contribution to  $g_{HBT}^{(2)}(0)$ ); as such, this value represents a lower bound, limited by the scattered laser and uncertainty in the temporal overlap of the short photon wavepackets at the beamsplitter.